Electronic Supplementary Information

Interfacial Engineered Surface Morphology Evolution of Au@Pd Core-Shell Nanorods

Yanchao Xu, Xiaoqiang Cui, Kun Qi, Shuting Wei, Qiyu Wang and Weitao Zheng**

State Key Laboratory of Automotive Simulation and Control, School of Materials Science and Engineering, Key Laboratory of Automobile Materials of MOE and Jilin University, Changchun, 130012, People's Republic of China

**Correspondence to: xqcui@jlu.edu.cn (X. Q. Cui) and wtzheng@jlu.edu.cn (W. T. Zheng)*

Contents:

Paraphrase of supersaturation

For the classic crystal growth theory, supersaturation was the primary driving force for both the nucleation and growth stages.[1] It was defined as the difference between the chemical potentials of the solute in solution and solid crystals at a particular value of the temperature, which is well-explained by the Thomson−Gibbs equation. In fact, this equation was originated from the thermodynamic equilibrium:

$$\Delta G = -SdT + VdP \qquad (1)$$

In the case of constant temperature T and pressure P ($dT = dP = 0$), the variation of Gibbs free energy (ΔG) of the crystal growth system gives:

$$\Delta G = \mu_l dn_l + \mu_c dn_c + \sigma dS = 0 \qquad (2)$$

Where S is the surface area of crystallites, n_l and n_c are the number of moles of solute in solution and solid crystals, respectively. Deduced from the above equation, the excess energy (the difference between $\mu_l dn_l$ and $\mu_c dn_c$) should convert to surface energy of crystallites (σdS) in the ideal case of constant temperature and pressure during crystal growth process.

Because $(n_l + n_c)$ were held constant for the whole crystal growth system, it would give $d(n_l + n_c) = 0$, and thus $dn_l = -dn_c$.

Then it will give:

$$\mu_l - \mu_c = \frac{\sigma dS}{dn_c} \qquad (3)$$

Considering a spherical crystallite (the radius is defined as h), the volume of crystal is $V = \frac{4}{3}\pi h^3 = n_c v$

Then $n_c = \frac{\frac{4}{3}\pi h^3}{v}$ and $dn_c = d\left(\frac{\frac{4}{3}\pi h^3}{v}\right) = \frac{4\pi h^2}{v}dh$

$$dS = d(4\pi h^2) = 8\pi h dh$$

$$\mu_l - \mu_c = \frac{\sigma dS}{dn_c} = \frac{\sigma(8\pi h dh)}{\frac{4\pi h^2}{v}dh}$$

As a result, , namely:

$$\Delta\mu = \mu_l - \mu_c = \frac{2\sigma v}{h} \qquad (4)$$

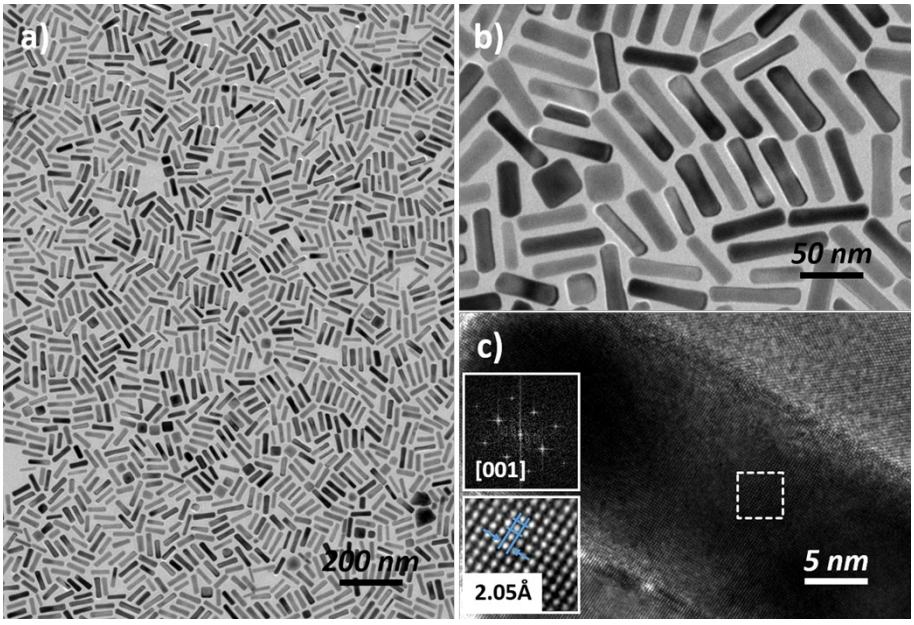

Figure S1. (a-c) TEM and HRTEM images of Au nanorod seeds. The inset of (c) shows the corresponding FFT pattern and the FFT refined HRTEM image of the region indicated by the white box in (c) recorded along the [001] zone axis.

TEM image shows that highly monodispersed Au nanorod seeds (the morphological yield can be over 95%) have been successfully prepared and no purification step was needed. As

shown in Fig S1c, the lattice distance is 0.205 nm, which is in good agreement with bulk Au (100) spacing. Furthermore, the FFT pattern in the inset of Fig S1c indicates a [001] direction, which also confirms a (100) facet.

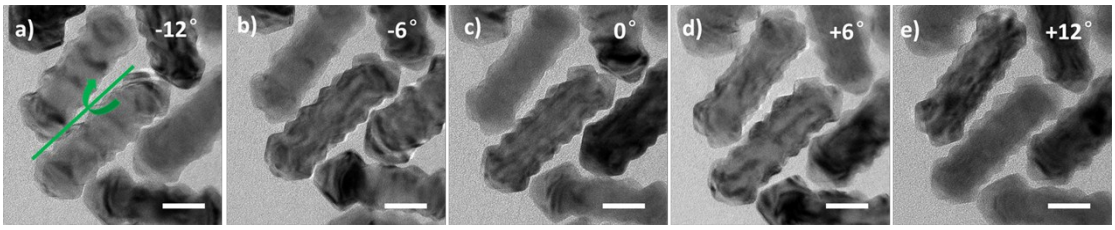

Figure S2. TEM images of Au@Pd core-island shell nanorods with different tilting angles. Scale bar: 10 nm.

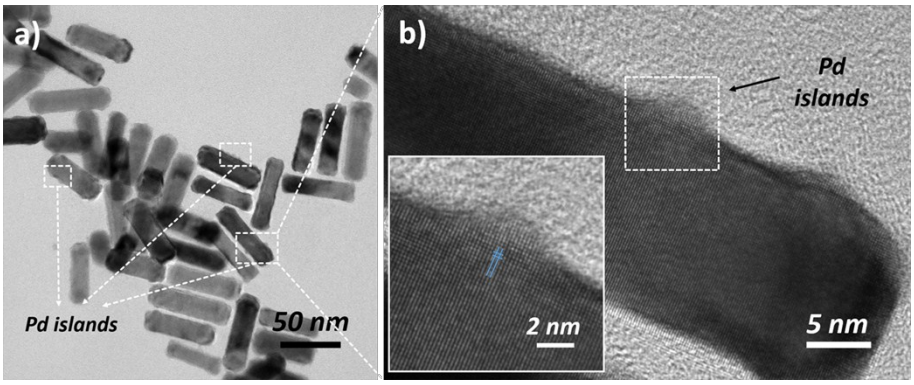

Figure S3. HRTEM images of Au@Pd nanorods with low Pd island coverage.

High-resolution transmission electron microscopy (HRTEM) images of both the Pd islands and Au nanorods shows coherent lattice fringes, suggesting an epitaxial growth of Pd islands on Au. Such an epitaxial growth not only prevents the production of defects, but aids the formation of well-crystallized interfaces.[2]

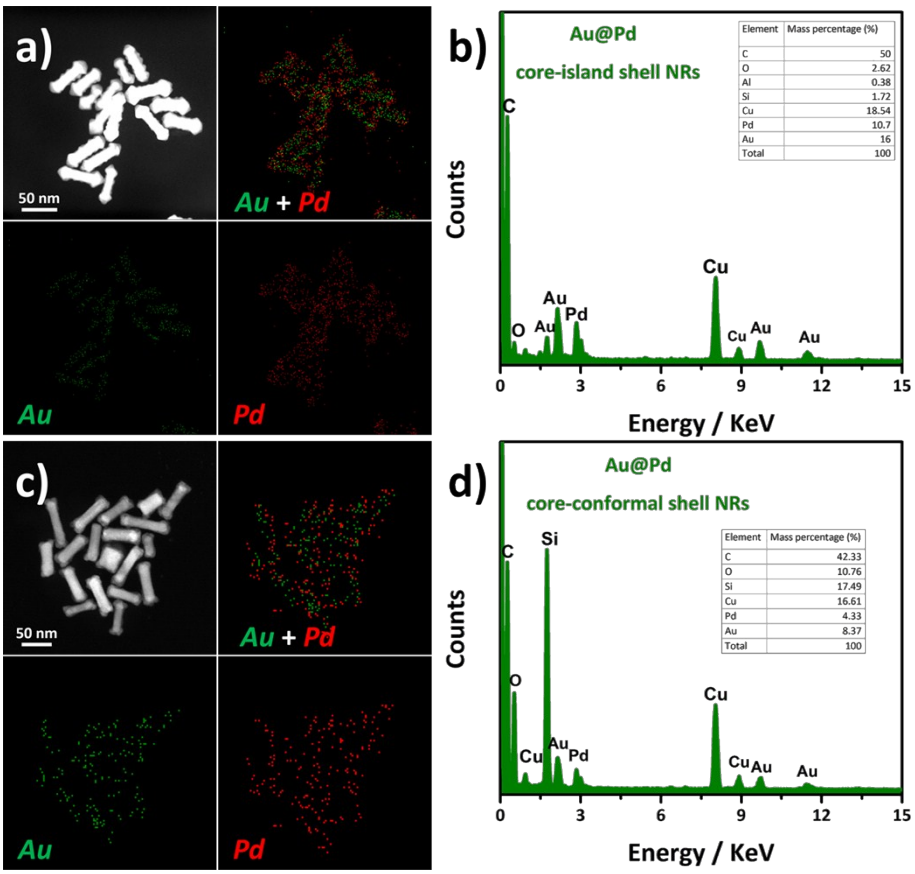

Figure S4. High angle annular dark field-scanning transmission electron microscopy (HAADF-STEM), element mapping and EDS spectrum: (a, b), Au@Pd core-island shell nanorods; (c, d), Au@Pd core-conformal shell nanorods.

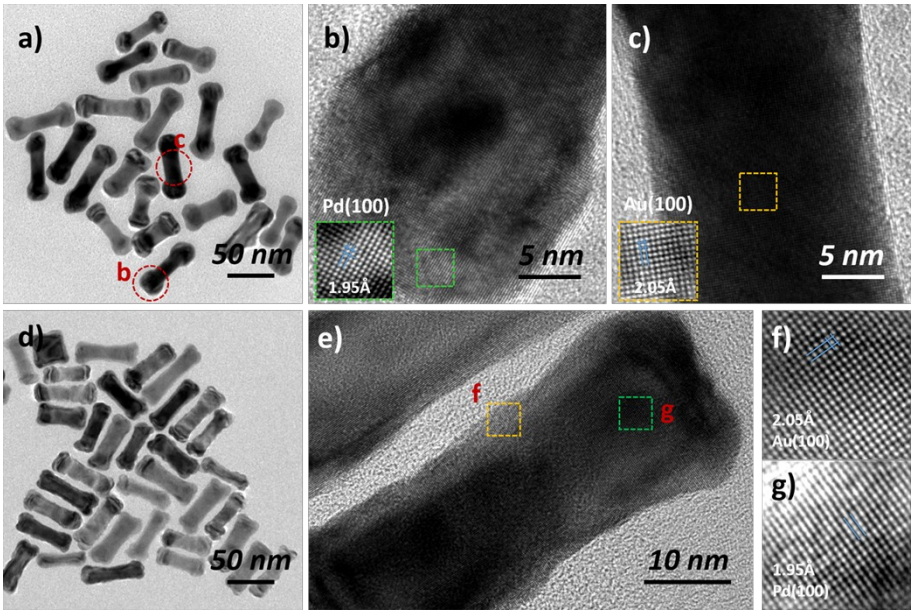

Figure S5. TEM and HRTEM images of Au@Pd binary nanorods mentioned in Figure 4a and 4c. HRTEM image indicates an epitaxial growth of Pd on Au.

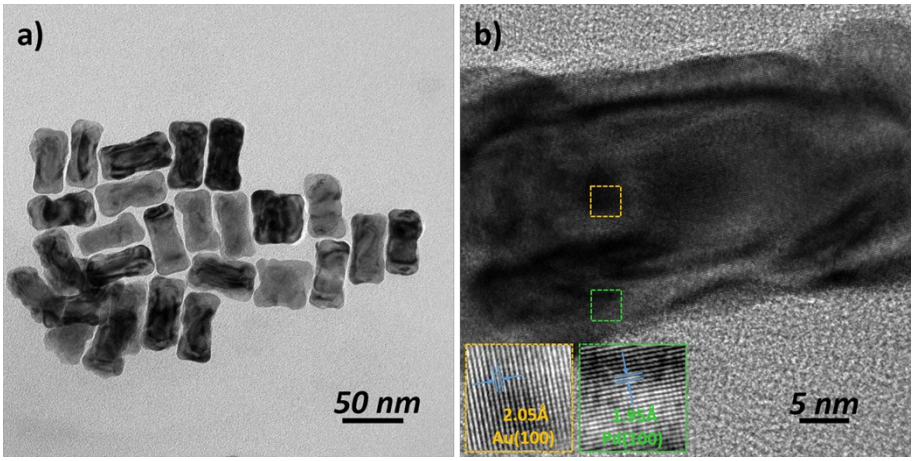

Figure S6. TEM and HRTEM images of Au@Pd binary nanorods mentioned in Figure 4f. HRTEM image indicates an epitaxial growth of Pd on Au.

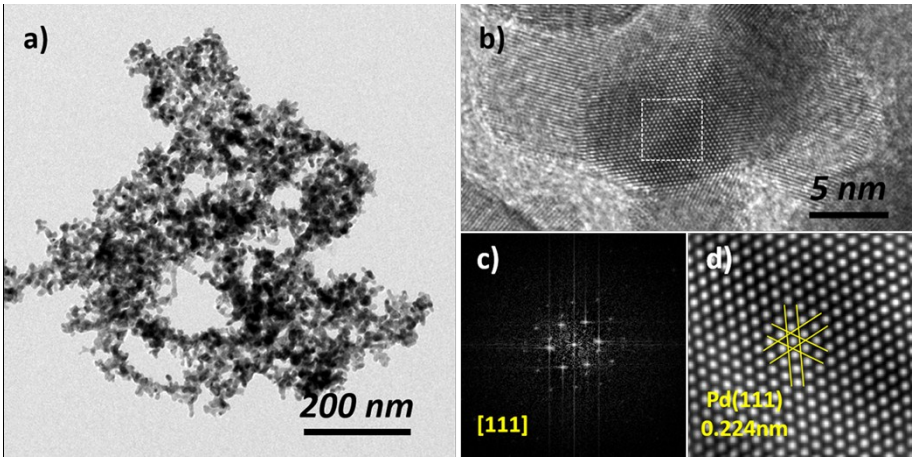

Figure S7. (a, b) TEM and HR-TEM characterization of Pd black. (c, d) Corresponding FFT pattern and the FFT refined HRTEM image of the region indicated by the white box in (b).

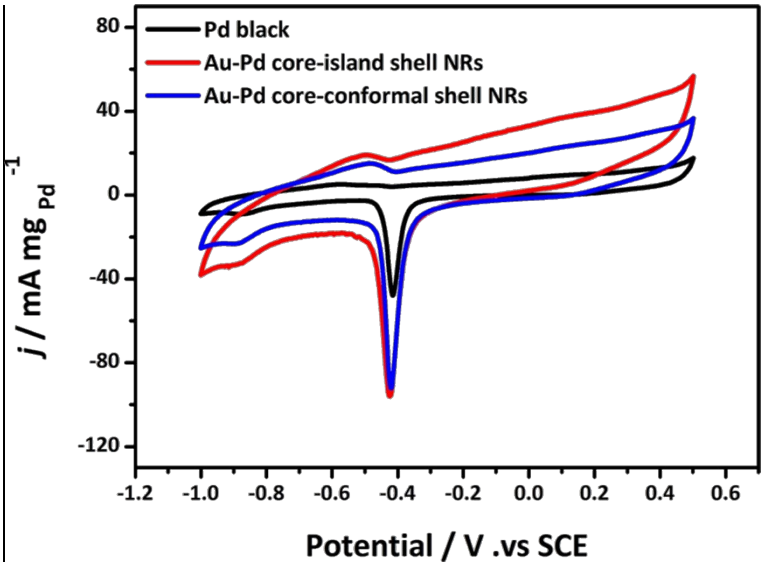

Figure S8. Blank cyclic voltammograms of three kinds of Pd-based catalysts recorded at room temperature in 1 M KOH (aq) without ethanol.

The CV curves were recorded at 50 mV s^{-1} after the curve was stable. The electrochemically active surface area (ECSA) of three kinds of catalysts was determined by integrating the surrounded by reduction peak of the palladium oxide and the CV baseline, which can be estimated by the following equation:

ECSA=Q_0/q_0,

Where Q_0 is the surface charge calculated from the area under the cyclic voltammetry scanning for oxygen desorption (-0.2–0.6 V vs. SCE) and q_0 is the charge required for desorption of monolayer of oxygen on the Pd surface (424 μC cm^{-2}).[3]

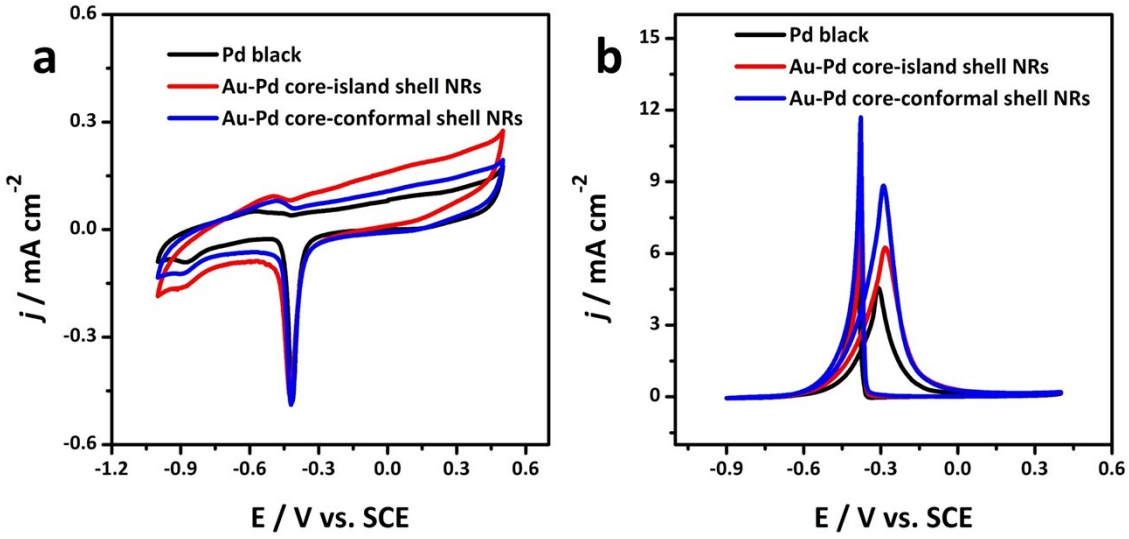

Figure S9. Cyclic voltammetry curves of three kinds of Pd-based catalysts in 1 M KOH. (b) Specific activity of three kinds of Pd-based catalysts in 1 M KOH + 1 M ethanol. Scan rate: 50 mV s^{-1}.

The oxidation peak current was normalized by the electrochemically active surface area (ECSA) to get the specific activity. The conformal-shell NRs exhibit the highest catalytic activity compared to the other structures. The specific activity of Au@Pd conformal-shell NRs was measured to be 8.8 mA cm^{-2}, which is 1.42 times and 2.00 times higher than those of Au@Pd island-shell NRs and Pd black catalysts, respectively.

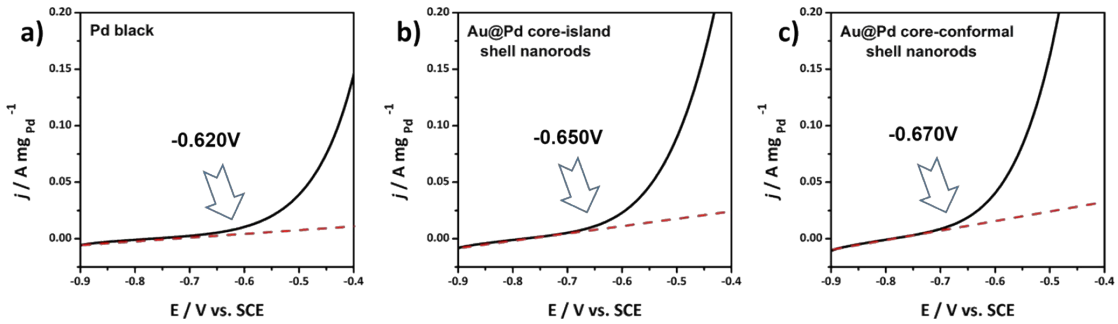

Figure S10. Amplified area of positive scanning in Figure 5a to distinguish the onset-potential of different Pd-based catalysts.

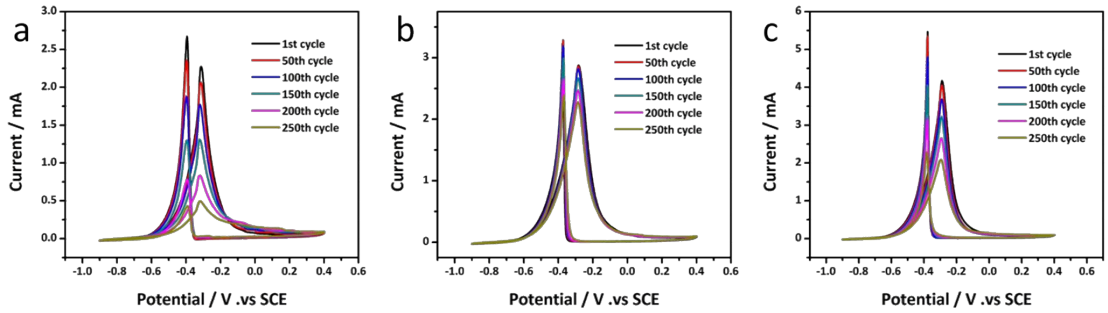

Figure S11. Cyclic voltammograms (1st, 50th, 100th, 150th, 200th and 250th cycle) of (a) Pd black, (b) Au-Pd core-island shell nanorods, (c) Au-Pd core-conformal shell nanorods for EOR . Potential was continuously scanned for 250 cycles at 50 mV s^{-1} in 1 M KOH + 1 M ethanol for EOR durability test.

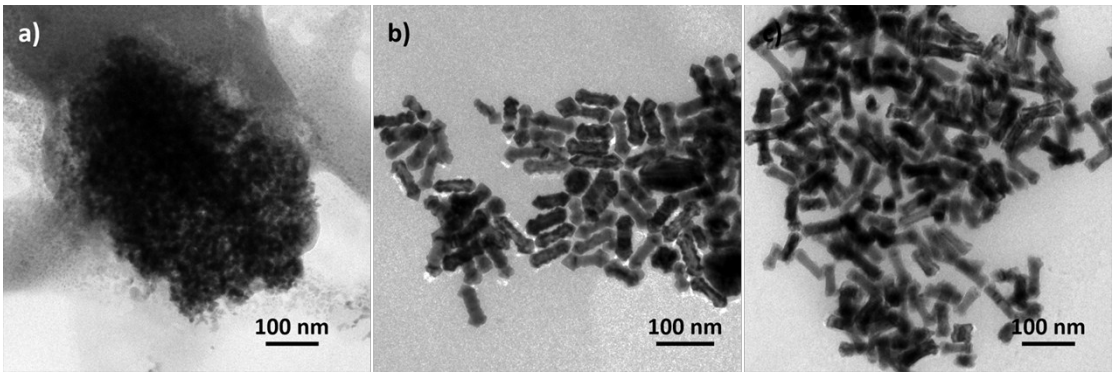

Figure S12. TEM images of three Pd-based catalysts after recyclability test: (a) Pd black; (b) Au@Pd core-island shell NRs and (c) Au@Pd core-conformal shell NRs.

As is shown in Fig. S12b-c, Au@Pd bimetallic nanorods showed a slight morphology change and aggregation after 250 cycles. As a comparison, the Pd black catalyst (Fig. S12a) obviously suffered from serious aggregation during the recyclability test, corresponding to the drastic decrease for its EOR activity.

Table S1. Specific surface free energy of *fcc* metals estimated by density of unsaturated bonds.

Facets	$\sigma_{h\,k\,l}$	$\sigma_{h\,k\,l}(\varphi_1/a^2)$
(111)	$\frac{1}{2}(3\varphi_1+3\varphi_2)/(\frac{\sqrt{3}}{4}a^2)$	3.81
(100)	$\frac{1}{2}(4\varphi_1+2\varphi_2)/(\frac{1}{2}a^2)$	4.20
(110)	$\frac{1}{2}(6\varphi_1+4\varphi_2)/(\frac{\sqrt{2}}{2}a^2)$	4.53

Table S1 shows the specific surface energy of the low-index crystallographic facets for fcc metals and it gives an order of σ(111)<σ(100)<σ(110). This result matched well with the previous report.[4]

Table S2.Detailed synthesis conditions for Au@Pd binary nanocrystals in this work.

	CTAB (mM)	*H_2PdCl_4 (μM)*	*H^+/OH^- (mM)*	*seed solution (μL)*	*AA (mM)*
Fig 2a	84	59	1.67 - H^+	500	3.37
Fig 1b&2b&3a&4b&4d	84	59	0.00	500	3.37
Fig 2c	84	59	0.84 - OH^-	500	3.37
Fig 1c&3b	84	59	3.37 - OH^-	500	3.37
Fig 1d	84	59	8.01 - OH^-	500	3.37
Fig 4a	84	59	0.00	500	0.86
Fig 4c	84	59	0.00	500	6.52
Fig 4e	84	128	0.00	500	3.37
Fig 4f	84	256	0.00	500	3.37

References

1. Lin, H. X.; Lei, Z. C.; Jiang, Z. Y.; Hou, C. P.; Liu, D. Y.; Xu, M. M.; Tian, Z. Q.; Xie, Z. X., Supersaturation-Dependent Surface Structure Evolution: From Ionic, Molecular to Metallic Micro/Nanocrystals. J. Am. Chem. Soc. 2013, 135 (25), 9311-9314.

2. Zheng, Z.; Tachikawa, T.; Majima, T., Single-Particle Study of Pt-Modified Au Nanorods for Plasmon-Enhanced Hydrogen Generation in Visible to Near-Infrared Region. J. Am. Chem. Soc. 2014, 136 (19), 6870-6873.

3. Hong, J. W.; Wang, S. W.; Choi, B. S.; Kim, D.; Lee, B. S.; Han, S. W., Controlled Synthesis of Pd–Pt Alloy Hollow Nanostructures with Enhanced Catalytic Activities for Oxygen Reduction. ACS Nano 2012, 6 (3), 2410-2419.

4. Lim, B.; Jiang, M.; Tao, J.; Camargo, P. H. C.; Zhu, Y.; Xia, Y., Shape-Controlled Synthesis of Pd Nanocrystals in Aqueous Solutions. Adv. Funct. Mater. 2009, 19 (2), 189-200.